



Bacterial outer membrane vesicle nanorobot

Songsong Tang^{a,b,1} , Daitian Tang^{a,c,d,1} , Houhong Zhou^{a,e,1} , Yangyang Li^{a,2}, Dewang Zhou^a, Xiqi Peng^{a,c,d} , Chunyu Ren^a, Yilin Su^{a,d}, Shaohua Zhang^{a,c} , Haoxiang Zheng^{a,c}, Fangchen Wan^a, Jounghyun Yoo^b , Hong Han^b , Xiaotian Ma^b , Wei Gao^{b,2} , and Song Wu^{a,c,d,2}

Affiliations are included on p. 11.

Edited by Joseph Wang, University of California San Diego, La Jolla, CA; received February 19, 2024; accepted June 5, 2024 by Editorial Board Member John A. Rogers

Autonomous nanorobots represent an advanced tool for precision therapy to improve therapeutic efficacy. However, current nanorobotic designs primarily rely on inorganic materials with compromised biocompatibility and limited biological functions. Here, we introduce enzyme-powered bacterial outer membrane vesicle (OMV) nanorobots. The immobilized urease on the OMV membrane catalyzes the decomposition of bioavailable urea, generating effective propulsion for nanorobots. This OMV nanorobot preserves the unique features of OMVs, including intrinsic biocompatibility, immunogenicity, versatile surface bioengineering for desired biofunctionalities, capability of cargo loading and protection. We present OMV-based nanorobots designed for effective tumor therapy by leveraging the membrane properties of OMVs. These involve surface bioengineering of robotic body with cell-penetrating peptide for tumor targeting and penetration, which is further enhanced by active propulsion of nanorobots. Additionally, OMV nanorobots can effectively safeguard the loaded gene silencing tool, small interfering RNA (siRNA), from enzymatic degradation. Through systematic *in vitro* and *in vivo* studies using a rodent model, we demonstrate that these OMV nanorobots substantially enhanced siRNA delivery and immune stimulation, resulting in the utmost effectiveness in tumor suppression when juxtaposed with static groups, particularly evident in the orthotopic bladder tumor model. This OMV nanorobot opens an inspiring avenue to design advanced medical robots with expanded versatility and adaptability, broadening their operation scope in practical biomedical domains.

nanorobots | bacterial outer membrane vesicle | enzyme propulsion | surface bioengineering

Nanorobotic technology is emerging as a revolutionary tool for precision diagnostics and therapy (1–6). Considerable efforts have been devoted to developing inspiring nanorobots propelled by chemical reactions or external energies (7–12). The steerable motion of nanomachines within confined spaces has shown promise in improving cellular diagnosis and treatment efficiency, including enhanced cellular internalization (13, 14), rapid intracellular sensing (15, 16), and effective drug delivery (17, 18). However, the building blocks of nanorobots mainly rely on rigid metal or inorganic materials [e.g., Pt (19), SiO₂ (20, 21), metal-organic frameworks (22), and polymers (23, 24)], suffering from compromised biocompatibility and biodegradability. On the other hand, the biological functions, such as tumor targeting, tissue penetration, and immune regulation, represent another aspect that enhances nanorobot performance in fulfilling medical missions (25, 26). Nevertheless, the inorganic body of current nanorobots only possesses inadequate inherent biofunctionality, barely meeting the demand for practical applications. For example, Au, SiO₂, and metal-organic frameworks (MOFs) exhibit acceptable biocompatibility and biodegradability (3, 27, 28). However, they lack the features of specific binding and penetration to biological tissues. Therefore, it is highly desirable to design fully biocompatible nanorobots with diverse intrinsic biological features.

To address these challenges, we introduce here autonomous urease-powered bacterial outer membrane vesicle (OMV) nanorobots. The surface-modified urease decomposes bioavailable fuel urea to effectively propel nanorobots. These nanorobots retain a variety of intrinsic properties and functionalities of nanoscale OMVs, including high biocompatibility, bacterial macromolecules [e.g., lipopolysaccharide (LPS), proteins, DNA, and peptidoglycan] for immune stimulation, and genetic bioengineering diversity to express specific functional proteins (29–31). The stable membrane structure also enables drug loading inside OMV nanorobots with reduced leakage and enzymatic degradation (32). The versatility and adaptability of OMV nanorobots enable wide applicability in various biomedical domains, including immunotherapy, vaccine development, and drug delivery. As an example, we designed a multifunctional OMV nanorobot for highly effective tumor therapy by harnessing the unique membrane features and autonomous propulsion (Fig. 1 *A* and *B*). The robotic OMV body

Significance

The compromised biocompatibility and biological features of present nanorobotic design have limited their development in biomedical community due to the dependence on inorganic materials. Here we integrate enzyme with bacterial outer membrane vesicle (OMV), yielding a fully biocompatible nanorobot that preserves the intrinsic properties of OMVs, including biocompatibility, immunogenicity, versatile surface bioengineering, cargo loading, and protection. The enzyme engine decomposes bioavailable fuel, urea inside the bladder, to propel nanorobots. The biofunctions of nanorobots are expanded by surface bioengineering with cell-penetrating peptide capable of tumor targeting and penetration. These behaviors are further enhanced by self-propulsion of nanorobots, inducing improved drug delivery efficacy and immune regulation. This work presents an advanced generation of nanorobots with expanded versatility for broader biomedical applications.

The authors declare no competing interest.

This article is a PNAS Direct Submission. J.W. is a guest editor invited by the Editorial Board.

Copyright © 2024 the Author(s). Published by PNAS. This article is distributed under [Creative Commons Attribution-NonCommercial-NoDerivatives License 4.0 \(CC BY-NC-ND\)](https://creativecommons.org/licenses/by-nc-nd/4.0/).

¹S.T., D.T., and H.Z. contributed equally to this work.

²To whom correspondence may be addressed. Email: liyangyang@zxiomed.org, weigao@caltech.edu, or wusong@szu.edu.cn.

This article contains supporting information online at <https://www.pnas.org/lookup/suppl/doi:10.1073/pnas.2403460121/-/DCSupplemental>.

Published July 15, 2024.

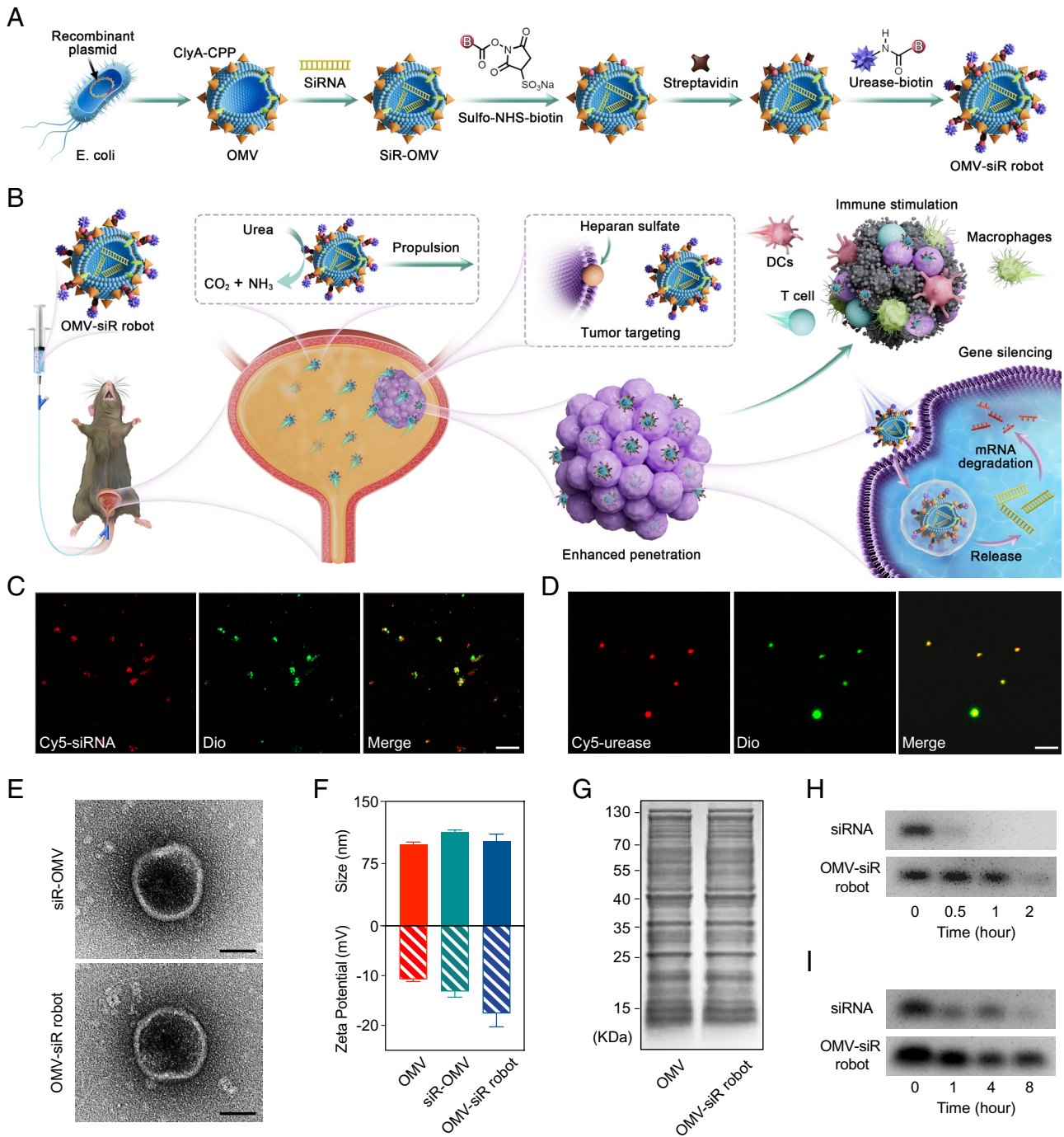


Fig. 1. Fabrication and characterization of OMV-siR robots. Schematic of (A) the fabrication process of OMV-siR robots with surface-bioengineered CPP capable of tumor-targeted binding and penetration, and (B) motion-enhanced gene silencing and immune stimulation for bladder cancer therapy. Fluorescence images showing the loaded siRNA (C) or modified urease (D) of OMV-siR robots in two independent experiments. siRNA or urease were labeled with Cy5 (red), respectively. The OMV body was stained with Dio (green). (Scale bar, 1.5 μm .) (E) TEM images of the siR-OMV and OMV-siR robot. (Scale bar, 100 nm.) (F) Hydrodynamic diameters and zeta potential of unmodified OMVs, siR-OMVs, and OMV-siR robots ($n = 3$; means \pm SD). (G) Gel electrophoresis analysis of proteins presented on unmodified OMVs and OMV-siR robots. The samples were run at equal protein content and stained with Coomassie blue. Gel electrophoresis analysis representing siRNA degradation of free siRNA or OMV-siR robots after exposure to RNase solution (H) or serum-containing medium (I) for various durations.

was genetically engineered with surface-expressing cell-penetrating peptide (CPP), capable of tumor targeting and penetration (33, 34). The tumor-targeting capability of CPP is attributed to their specific recognition and binding to heparan sulfates expressed on the surface of tumor cells or tumor vessels (34). Additionally, the membrane structure of nanorobots offered effective protection for the loaded gene silencing tool, small interfering RNA (siRNA), from enzymatic degradation. Moreover, the biocatalytic propulsion enhanced the specific binding and penetration of siRNA-loaded

OMV nanorobots (OMV-siR robots) to the tumor site. Our in vivo evaluation of such OMV-siR robot demonstrated enhanced siRNA delivery and immune regulation, further resulting in the highest antitumor efficacy against the orthotopic bladder tumor model, in contrast to other static constructs. These OMV nanorobots represent a promising avenue to develop next-generation medical nanorobots with expanded versatility, holding considerable potential to meet the rigorous requirements of various in vivo biomedical applications.

Results

Fabrication and Characterization of OMV-siR Robots. Fig. 1A shows the fabrication process of OMV-siR robots. The recombinant plasmid was first constructed by integrating the gene segments of Cytolysin A (ClyA) protein, hexahistidine (6xHis) tag with CPP protein using a commercial vector (pET28a, *SI Appendix, Fig. S1A*), then transformed into competent *Escherichia coli* (*E. coli*, BL21). The bioengineered bacteria produced OMVs with outer membrane protein CPP (OMV-CPP) upon ultrasound stimulation. Western blot analysis revealed distinct bands of 6xHis-CPP protein in bioengineered bacteria and OMV-CPP (*SI Appendix, Fig. S1B*). In contrast, the CPP band was absent in wild-type bacteria and produced OMVs (OMV-WT), verifying the successful expression of CPP in both bioengineered bacteria and OMV-CPP. The transmission electron microscopy (TEM) images showed that such genetical engineering did not alter the morphology and size (around 108.4 nm) of OMV-CPP compared to OMV-WT (*SI Appendix, Fig. S1C*). Afterward, OMVs-CPP were loaded with siRNA through electroporation. The resulting siRNA-loaded OMVs-CPP (siR-OMV) were sequentially reacted with sulfo-N-hydroxysuccinimide (NHS)-biotin, streptavidin, and urease-biotin to modify urease on OMV membrane, generating urease-powered OMV-siR robots. The strong noncovalent binding of biotin–streptavidin–biotin complex offers robust conjugation between the OMV surface and urease, yielding a stable robotic engine for diverse applications in biological environments. The increased chain length of this two-step surface modification may create a broader space for enzyme immobilization on the OMV surface, thereby introducing a larger quantity of enzyme with enhanced catalytic movement.

The successful siRNA loading and urease modification were verified by fluorescence characterizations (Fig. 1C and D). In independent experiments, Cyanine5 (Cy5, red)-labeled siRNA or urease displayed colocalized fluorescence with OMV nanorobots that stained with 3,3'-diiodoacetylcarboxycyanineperchlorate (Dio, green). The TEM image of OMV nanorobot exhibited similar morphology and size in contrast with siR-OMV (Fig. 1E).

The hydrodynamic diameter and zeta potential of OMV-siR robots were examined as 115.7 nm and -20.4 mV (Fig. 1F). The gel electrophoresis analysis showed that the protein profile of nanorobots closely matched to that of siR-OMVs (Fig. 1G). These findings indicate the negligible effect of electroporation and surface modification on the membrane structure and protein contents of OMV-siR robots. The intact membrane of nanorobots was also verified with the function to protect loaded siRNA from degradation by RNases (Fig. 1H) and serum (Fig. 1I). The siRNA bands remained clearly visible after incubating nanorobots with RNases for 1 h or serum-containing medium for 8 h. Whereas the bands of free siRNA disappeared after exposure to RNases solution for 0.5 h or serum solution for 8 h. Overall, these results demonstrate the successful construction of OMV-siR robots that preserve intrinsic protein profiles of OMVs and bioengineered CPP. The intact membrane integrity of nanorobots also enables the protection of loaded siRNA from enzymatic degradation.

Motion Study. The immobilized urease on the membrane of OMV nanorobots can decompose urea into carbon dioxide and ammonia. The uneven distribution of urease on OMV surface is inevitable during the surface modification (35). Thus, such biocatalytic decomposition generates asymmetric distribution of reaction products with directional flow, inducing self-diffusiophoretic propulsion for nanorobots (36–38).

The motion performance of OMV-siR nanorobots was first examined in phosphate-buffered saline (PBS) solution containing different urea concentrations (0, 50, 100, and 200 mM). The movement of nanorobots was enhanced with elongated propulsion trajectories by rising urea concentration (Fig. 2A and *Movie S1*). The mean square displacement (MSD) of nanorobots was calculated with linear growth over time and improved upon the increasing urea concentrations (Fig. 2B). Accordingly, the measured diffusion coefficient (D_{eff} ; Fig. 2C) and speed (Fig. 2D) were also improved at higher urea concentration. We also evaluated the movement of unmodified OMVs in PBS solution with various urea concentrations (*SI Appendix, Fig. S2* and *Movie S2*). As expected, only Brownian motion was detected for unmodified

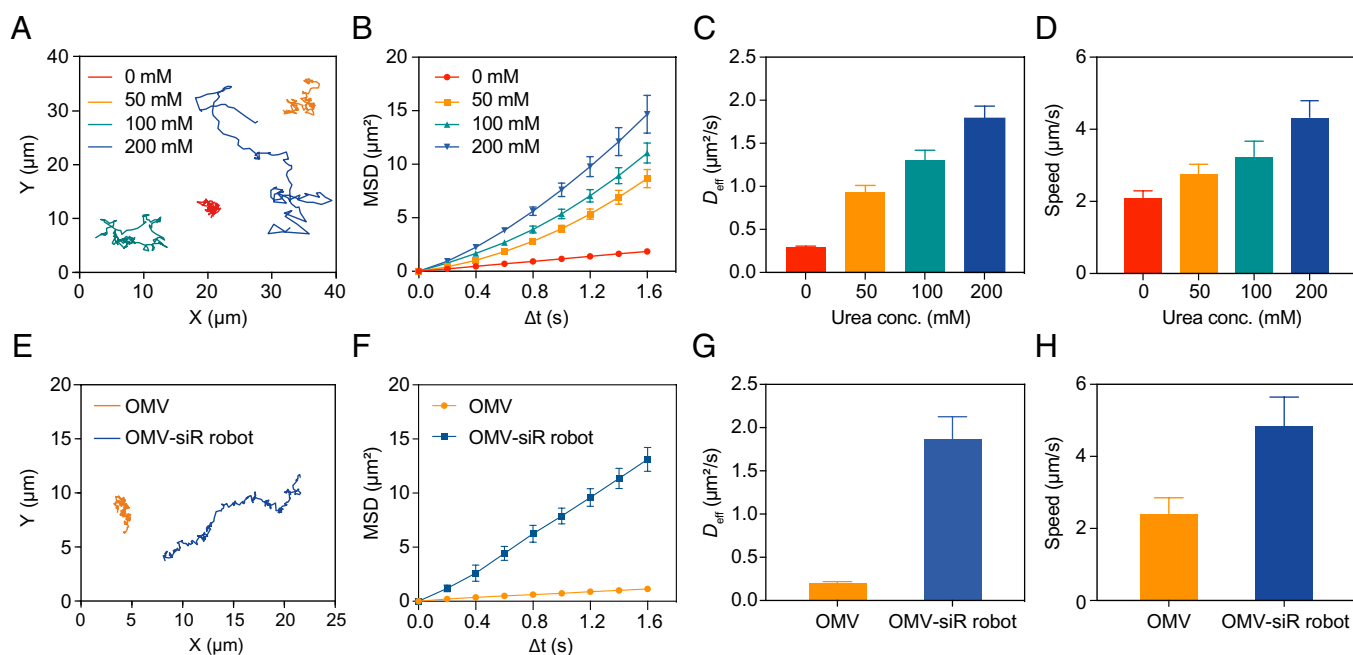


Fig. 2. Motion performance of OMV-siR robots. (A) Typical motion trajectories (over 25 s), (B) MSD, (C) diffusion coefficient (D_{eff}), and (D) speed of OMV-siR robots in PBS solution with various urea concentrations ($n = 15$; means \pm SEM). (E) Typical motion trajectories (over 25 s), (F) MSD, (G) D_{eff} , and (H) speed of unmodified OMVs and OMV-siR robots in real urine, collected from mice bearing the orthotopic bladder tumor ($n = 15$; means \pm SEM).

OMVs due to the lack of catalytic engine. Afterward, the motion performance of nanorobots over extended periods of time was assessed in PBS solution containing 200 mM urea. The movement was examined at various time points, including 0, 8, 16, and 24 h (*SI Appendix, Fig. S3 and Movie S3*). The motility of the nanorobots significantly decreased and reached the level of Brownian motion after 16 h, attributed to the depletion of urea fuel. Fresh 200 mM urea was added at the timepoint of 24 h, leading to distinct motility recovery of nanorobots. These results demonstrate the favorable capability of nanorobots to maintain movement over extended durations.

The high urea concentration in human (up to 285 mM) or mouse (up to 1,800 mM) urine offers sufficient fuel to propel urease-powered nanorobots (39). We further evaluated the propulsion performance of unmodified OMVs and OMV-siR robots in real urine (Fig. 2 *E–H* and *Movie S4*), collected from the mice bearing orthotopic bladder tumors. The urea concentration in collected mice urine was detected as 448.0 ± 26.6 mM. The nanorobots showed effective movement in urine solution, whereas only Brownian motion was observed for unmodified OMVs.

The stability of nanorobots was also assessed by examining the enzyme fluorescence and motion performance after storage at 4 °C for 7 d. The movement of nanorobots was evaluated in PBS solution containing 200 mM urea after storage. The nanorobots after stored for 1 and 7 d exhibited comparable motion performance in contrast with newly prepared nanorobots (*SI Appendix, Fig. S4 A–C*). The fluorescence images demonstrated that Cy5-labeled urease remained attached onto the surface of nanorobots after 7-d storage (*SI Appendix, Fig. S4D*). These results suggest the superior construction stability of fabricated nanorobots. The capability of nanorobots to move in the bioavailable fuel and their construction stability are prerequisite to accomplish biomedical missions in practical biological environments, such as the bladder.

siRNA Loading and Release. Survivin is a unique protein of the inhibitor of apoptosis families in mammalian cells. The overexpression of survivin has been widely found in tumor cells, which is involved in suppressing cell apoptosis (40). Here, we selected survivin as the gene silencing target due to its pivotal role in cell death regulation. We first assessed the expression levels of survivin in various cells, including human uroepithelial cells (SV-HUC-1), mouse brain endothelial cells (bEnd.3), mouse bladder carcinoma cells (MB49 and MBT-2), using Western blotting analysis (*SI Appendix, Fig. S5A*). The highest survivin expression was detected in MBT-2 cells, which was used to establish the orthotopic bladder tumor model in our study. The siRNA-810 against survivin was selected as the payload for nanorobots, which was verified with effective inhibition on MBT-2 cell growth after incubation for 3 d, compared to the negative control siRNA (siRNA-NC) and siRNA-257 (*SI Appendix, Fig. S5B*). This indicates the function of siRNA-810 in silencing survivin expression and further inducing cell apoptosis.

Next, the drug loading capacity of nanorobots was evaluated upon various siRNA inputs. The peak loading efficiency (64.5%) was achieved at the input of 1 μ M (Fig. 3*A*), corresponding to a loading amount of 0.645 μ M (*SI Appendix, Fig. S6*), which was optimized as the fabrication condition for OMV-siR robots. The siRNA release profile of nanorobots was assessed in PBS solution with different pH values (Fig. 3*B*). Only slow drug release was observed in both conditions, attributed to the protective membrane structure of OMV nanorobots. The cellular uptake of OMV-siR robots is expected to facilitate the release of most siRNA into the cytoplasm.

In Vitro Gene Silencing Effect. The robotic body OMV was examined with favorable biocompatibility and negligible toxicity to different cells, including SV-HUC-1, bEnd.3, and MBT-2 cells, within the concentration of 44 μ g/mL (*SI Appendix, Fig. S7*), which

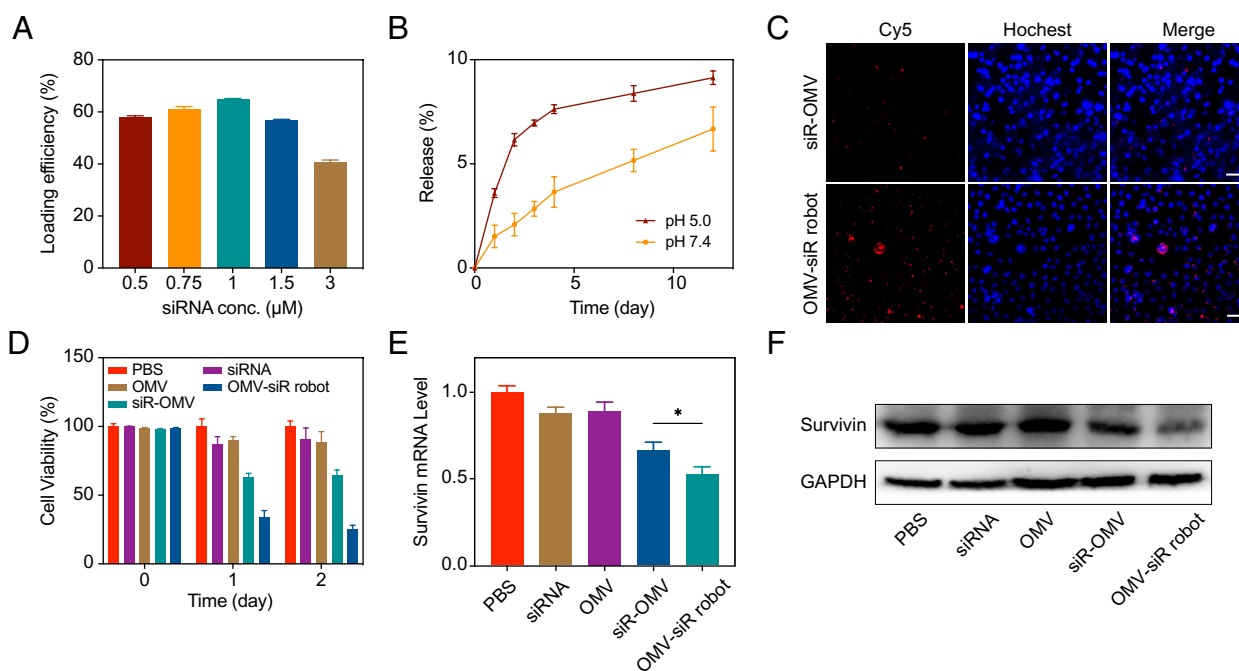


Fig. 3. Drug loading and release profiles, and in vitro anticancer effect of OMV-siR robots. (A) Loading efficiency of OMV-siR robots upon different siRNA inputs ($n = 3$; means \pm SD). (B) Cumulative siRNA release from OMV-siR robots at pH 5.0 or 7.4 over 12 h ($n = 3$; means \pm SD). (C) Fluorescence images of MBT-2 cells after incubation with siR-OMVs or OMV-siR robots for 2 h in the presence of 100 mM urea. Cells and siRNA were labeled by Hoechst 33342 (blue) and Cy5 (red), respectively. (Scale bar, 10 μ m.) (D) Viability of MBT-2 cells after first incubation with various solutions for 2 h at 100 mM urea, including PBS, siRNA, OMVs, siR-OMVs, and OMV-siR robots, then separation for another 22 or 46-h incubation ($n = 3$; means \pm SD). (E) Relative survivin mRNA expression in MBT-2 cells after incubation with nanorobots and other control groups for 2 h at 100 mM urea, followed by isolation for another 22-h culture ($n = 3$, mean \pm SD). (F) Western blot for survivin in MBT-2 cells after culture with nanorobots and other constructs for 2 h at 100 mM urea, then separated to incubate for 46 h; glyceraldehyde-3-phosphate dehydrogenase (GAPDH) was used as loading control. * $P < 0.05$; one-way ANOVA.

was the application range in this work. The toxicity of OMV-based nanorobots to MBT-2 tumor cells at higher concentration (88 $\mu\text{g}/\text{mL}$) might be attributed to their tumor-specific binding enabled by bioengineered CPP-ClyA fusion protein on the surface of nanorobots. This led to overaggregation of the cytotoxic ClyA protein on the tumor site, resulting in decreased cell viability (41, 42).

We further evaluated the loaded siRNA function after electroporation. The commercial liposomes were employed to loaded siRNA (siR-Lipo) through coculture without affecting siRNA property, serving as the counterpart. MBT-2 cells were incubated with siR-Lipo and OMV-siR robots at the same siRNA concentration for 24 h. The expression level of survivin mRNA inside MBT-2 cells was examined using PCR. In comparison to the PBS group, both the siR-Lipo and nanorobot groups exhibited inhibited mRNA expression levels, with comparable levels between the two groups (*SI Appendix, Fig. S8*). This suggests the negligible impact of electroporation on the loaded siRNA effectiveness within OMV-siR robots.

To determine the function of active propulsion in the binding efficiency of nanorobots to cancer cells, both nanorobots and siR-OMVs, loaded with Cy5-labeled siRNA at an equivalent OMV concentration (44 $\mu\text{g}/\text{mL}$), were incubated with MBT-2 cells for 2 h at 100 mM urea (*Fig. 3C*). In this study, the urea concentration of 100 mM was selected as the propulsion fuel for in vitro tests because the motion performance of nanorobots in mice urine (*Fig. 2F*) was comparable to that in PBS solution containing 100 mM urea (*Fig. 2B*). Although the urea concentration within mouse urine (448.0 mM) was significantly higher than 100 mM, the complex components of real urine, which includes protein, DNA, RNA, and other metabolic impurities, could potentially impact the motion of nanorobots. The cell nuclei were stained with Hoechst 33342. Stronger red fluorescence was observed on the cell surface after incubation with nanorobots compared to the siR-OMV group, suggesting the role of nanorobot propulsion in enhancing their binding with cells.

To evaluate the in vitro anticancer effect, MBT-2 cells were incubated with various solutions for 2 h, including PBS, free siRNA, unmodified OMVs, siR-OMVs, and OMV-siR robots, followed by removing suspension and adding fresh cell culture medium for another 22 or 46-h incubation (*Fig. 3D*). Nanorobots induced the lowest cell viability (23.1%) in contrast with other static groups. The cell apoptosis was also explored by annexin V/PI staining. Flow cytometry analysis showed the highest cell apoptosis ratio (47.93%) in the nanorobot group (*SI Appendix, Fig. S9*). To elucidate the cell death mechanism, we first examined the expression level of survivin mRNA. This two-dimensional (2D) cell culture enabled the cellular uptake of passive OMV counterparts in a certain amount. Thereby, the survivin mRNA expression was inhibited in the group of siR-OMV compared to the OMV group (*Fig. 3E*). The smallest mRNA level (54.9%) was detected in the MBT-2 cells that incubated with nanorobots. Western blotting analysis was further performed to assess the expression of survivin protein (*Fig. 3F*). OMV-siR robots significantly suppressed survivin expression compared to other control groups. These results indicate that the effective propulsion of OMV nanorobots could enhance their binding to cancer cells, further improving siRNA delivery and gene knockdown efficacy.

Tumor-Targeted Binding and Penetration. We first sought to verify the intrinsic tissue penetration capability of OMV-CPP. The three-dimensional (3D) bladder tumor cell spheroid was built using MBT-2 cells and then incubated with OMV-WT or OMV-CPP overnight. OMVs and MBT-2 cells were labeled with

1,1'-Diocadecyl-3,3,3',3'-tetramethylindocarbocyanine perchlorate (Dil, red) and Hoechst 33342 (blue), respectively. Confocal laser scanning microscopy (CLSM) was used to explore the fluorescence distribution of cell spheroids at various depths (*SI Appendix, Fig. S10A*). Dil-labeled OMV-WT mainly distributed on the cell spheroid surface. In contrast, distinct red fluorescence of OMV-CPP was observed within the internal areas of cell spheroid. Then, the bladder mucosa of mice was resected to incubate with Dil-labeled OMV-WT or OMV-CPP for 2 h (*SI Appendix, Fig. S10B*). The bladder mucosa was stained with Hoechst 33342 (blue). The red fluorescence of OMV-CPP colocalized with deeper tissue layers, but the OMV-WT fluorescence primarily confined to the mucosa surface. These results demonstrate the unique property of bioengineered CPP on OMV membrane in enhancing tissue penetration.

Next, the binding specificity to tumor cells of nanorobots was examined by incubating Dil-labeled nanorobots with various cells in the presence of urea (100 mM) for 2 h (*Fig. 4A*). The strongest red fluorescence was noted on the surface of MBT-2 bladder cancer cells (*Fig. 4B and C*), in contrast with the scarce red fluorescence on SV-HUC-1 and bEnd.3 cells. This binding affinity confirms the tumor-targeting capability of OMV nanorobots by leveraging the inherent feature of bioengineered CPP (43). On the other hand, comparable red fluorescence was observed when Dil-labeled nanorobots were incubated with T24 and MBT-2 bladder tumor cells (*SI Appendix, Fig. S11*), indicating the nonselective binding of nanorobots to various tumor cells (34). The tissue penetration of nanorobots was assessed by culturing Dil-labeled siR-OMVs or OMV-siR robots with Hoechst 33342-stained bladder cancer cell spheroids in 100 mM urea for 2 h (*Fig. 4D*). Rare fluorescence of static siR-OMVs was found on the surface of cell spheroid due to the lack of motility (*Fig. 4E*). Whereas the nanorobot group exhibited obvious red fluorescence on the cell spheroid with deep fluorescence infiltration, attributed to the synergistic effect of active propulsion and bioengineered CPP. The quantified fluorescence at various depths of cell spheroids is shown in *SI Appendix, Fig. S12*.

We further evaluated the in vivo tumor targeting and penetration behavior of nanorobots using the mice bearing orthotopic bladder tumor model. Dil-labeled urease-modified OMV-WT, siR-OMVs, or OMV-siR robots were intravesically injected and incubated for 2 or 12 h (*Fig. 4F*). As a widely used clinical procedure for treating bladder cancer, intravesical instillation enables rapid and facile entry of nanorobots into the bladder chamber at desired concentrations (44). This in situ administration of nanorobots bypasses other organs to reach the bladder directly, thereby minimizing the potential side effects on other organs. Then, the bladder tumor was resected for slicing and stained with Hoechst 33342. The tumor area was marked with dash lines (*Fig. 4G and SI Appendix, Fig. S13*). After 2-h incubation, most siR-OMVs existed in the bladder cavity due to the motion deficiency. The red fluorescence of urease-modified OMV-WT mostly located on the bladder wall (*SI Appendix, Fig. S13*), resulted from their random propulsion without targeted navigation. In contrast, large amount of nanorobots attached to the tumor surface with significant fluorescence penetration into the tumor tissue (*Fig. 4G*). After 12 h, only weak fluorescence of siR-OMVs colocalized with the bladder tumor. The effective propulsion of urease-immobilized OMV-WT led to enhanced retention in the bladder wall rather than penetration into the tumor tissue. Whereas OMV nanorobots induced distinct fluorescence penetration into deeper tumor tissue. These results demonstrate that the biocatalytic propulsion of nanorobots can significantly enhance their tumor-specific binding and penetration that leverages the CPP function.

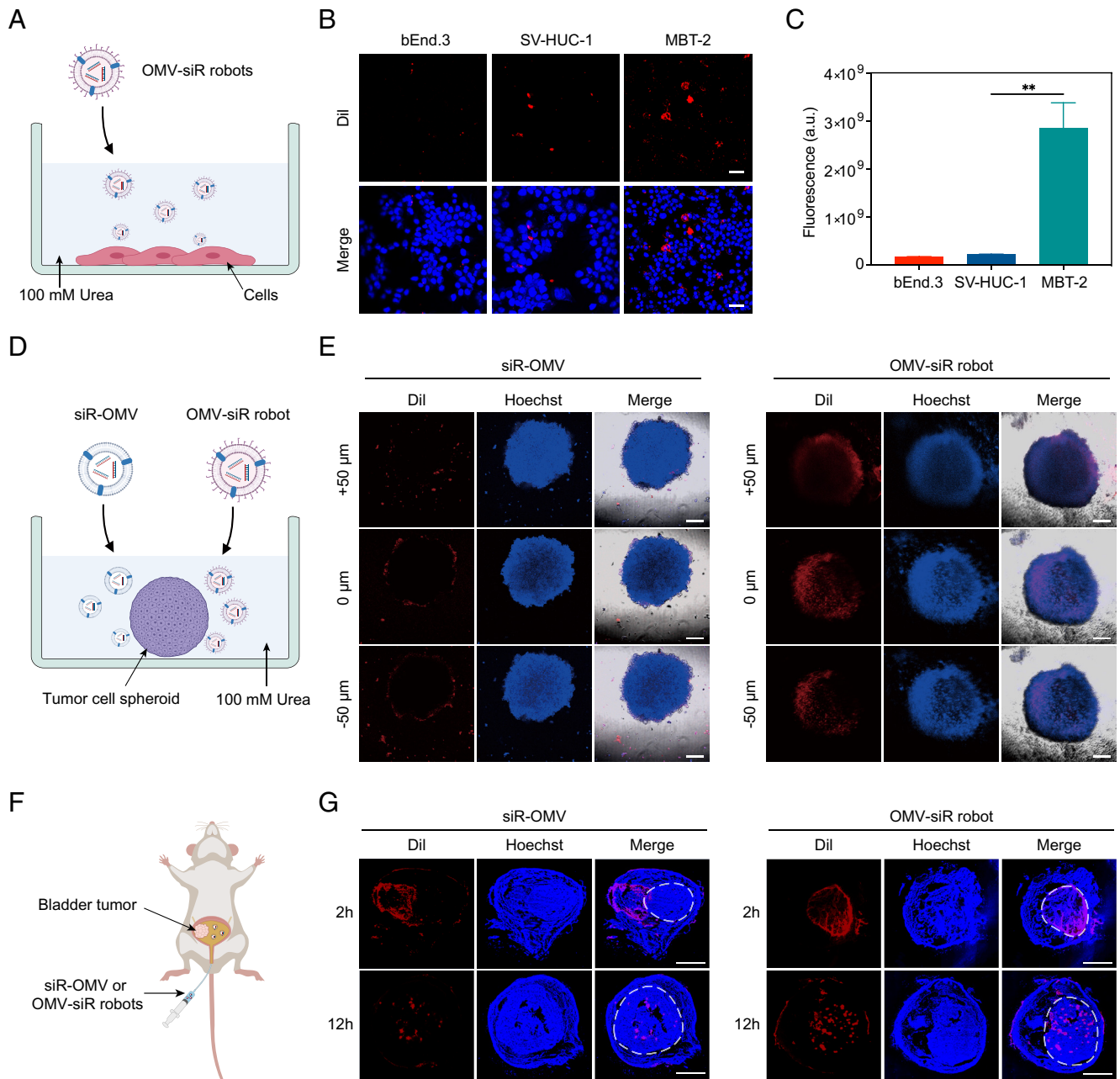


Fig. 4. In vitro and in vivo evaluation of tumor targeting and penetration of OMV-siR robots. (A) Schematic, (B) fluorescence images, and (C) quantified Dil fluorescence intensity showing the binding affinity of OMV-siR robots after incubation with various cells for 2 h in the presence of 100 mM urea, including bEnd.3 mouse brain endothelial cells, SV-HUC-1 human uroepithelial cells and MBT-2 mouse bladder carcinoma cells. Cells and nanorobots were stained by Hoechst 33342 (blue) and Dil (red), respectively. (Scale bar, 10 μ m.) (D) Schematic and (E) fluorescence images representing the adhesion and penetration of siR-OMV or OMV-siR robots to MBT-2 cell spheroids after cocultivation for 2 h at 100 mM urea. OMV membranes and cell spheroids were stained with Dil (red) and Hoechst 33342 (blue), respectively. The fluorescence images of cell spheroids were captured at various depths. (Scale bar, 20 μ m.) (F) Schematic and (G) Fluorescence images showing the distribution of siR-OMV or OMV-siR robots after intravesical instillation to the mouse bearing orthotopic bladder tumor for 2 or 12 h. OMVs and bladder tumor tissues were stained with Dil (red) and Hoechst 33342 (blue), respectively. (Scale bar, 1 mm.)

In Vivo Anticancer Efficacy of OMV-siR Robot. After confirming the active tumor targeting and penetration behaviors of OMV-siR robots inside tumor-bearing bladder, we sought to explore the effect of these nanorobot-enabled improvements on immune regulation and gene silencing. The mice bearing orthotopic MBT-2 bladder tumor were established and intravesically instilled with PBS, unmodified OMVs, siR-OMVs, and OMV-siR robots (Fig. 5A). On day 15, the immune stimulation and gene silencing were examined by detecting the recruitment of immune cells and survivin expression in resected tumor tissues, respectively. As shown in Fig. 5B–E, the injection of OMV-siR robots notably

increased the percentages of mature dendritic cells (DCs, Fig. 5B and *SI Appendix, Fig. S14A*), CD4⁺ T helper cells (Fig. 5C and *SI Appendix, Fig. S14B*), CD8⁺ cytotoxic T lymphocytes (Fig. 5D and *SI Appendix, Fig. S14C*) and macrophages (Fig. 5E and *SI Appendix, Fig. S14D*) in contrast with other groups. The levels of proinflammatory cytokines, including interferon- γ (IFN- γ , Fig. 5F), tumor necrosis factor α (TNF- α , Fig. 5G), and interleukin 6 (IL-6, Fig. 5H), were also elevated by nanorobots. Then, the siRNA delivery efficacy was evaluated by assessing the survivin expression in tumor tissues. Western blot analysis displayed comparable survivin expression within bladder tumor cells in the

groups of PBS, OMV, and siR-OMV. This was attributed to the small amount of passive OMV and siR-OMV that could bind to the tumor site in the 3D tumor model. The lowest survivin expression was detected in the group of OMV-siR robots (Fig. 5I). Such inhibited expression of survivin was further confirmed by the immunohistochemistry staining (Fig. 5J). The brown color representing survivin protein was rarely observed in the tumor tissue treated with OMV-siR robots. These results demonstrate the function of nanorobots in enhancing immune response and gene silencing in an orthotopic bladder tumor model due to the motion-enhanced tumor-targeted binding and penetration inside the bladder.

We further evaluated the therapeutic efficacy of OMV nanorobots against the orthotopic MBT-2 bladder tumor model using the same experimental settings (Fig. 6A). The tumor-bearing mice were intravesically instilled with OMV-siR robots and other control groups. The tumor growth was monitored by the bioluminescence signal of luciferase-expressing MBT-2 cells (Fig. 6B and C and *SI Appendix*, Fig. S15) during the treatment process. Negligible fluorescence was detected on the mice after treated with OMV-siR robots on day 28, while the mice in other groups still showed obvious fluorescence. Mice mortality was found in all groups except the nanorobot group (Fig. 6D). The bladder tumor tissues were resected after the treatment course (Fig. 6E). As shown in Fig. 6F, the OMV group exhibited tumor-killing effect compared to the PBS group, due to their inherent

immunogenicity. The pathogen-associated molecular patterns of OMVs could elicit the antitumor immune response by recruiting and activating immune cells toward antitumor phenotypes (Fig. 5B–E) (45–47). The group of OMV-siR robots had the lowest tumor tissue weight (Fig. 6F). The collected tumor tissues were further processed with histological staining, including hematoxylin and eosin (H&E, Fig. 6G), terminal deoxynucleotidyl transferase-mediated deoxyuridine triphosphate nick end labeling (TUNEL), and Ki67 (*SI Appendix*, Fig. S16). The intravesical administration of OMV-siR robots induced much smaller tumor size, significant cell necrosis, and apoptosis with inhibited proliferation index compared to other constructs. These results verify the capability of self-powered OMV nanorobots to effectively inhibit bladder tumor growth, attributed to their active tumor targeting and penetration behavior.

Last, we assessed the in vivo biosafety of OMV-siR robots. No significant weight change occurred on the mice (Fig. 6H). The major serum biomarkers of mice were detected within normal ranges, including serum aspartate transaminase (AST, Fig. 6I), alanine transaminase (ALT, *SI Appendix*, Fig. S17), blood urea nitrogen (BUN, Fig. 6J), alkaline phosphatase (ALP, Fig. 6K), and lactate dehydrogenase (LDH, Fig. 6L). In addition, the main organs, heart, liver, spleen, lung, and kidney, were processed with H&E staining (*SI Appendix*, Fig. S18). The administration of the nanorobots did not affect the overall integrity and structure of these organs compared to the control group. Overall, these results

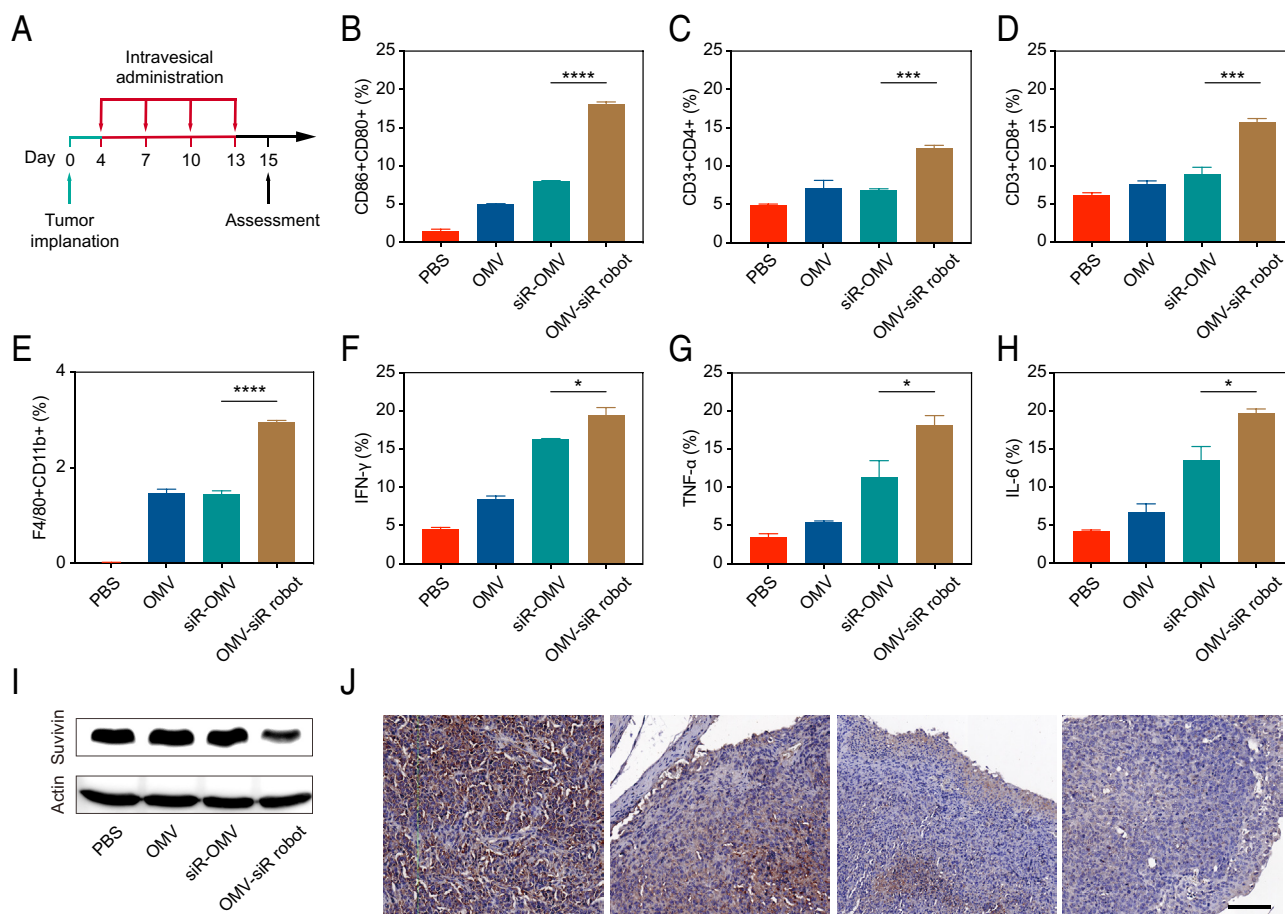


Fig. 5. In vivo immunomodulation and gene silencing of OMV-siR robots. (A) Schematic of the treatment course of mice bearing orthotopic MBT-2 bladder tumor, where the effects of immune stimulation and gene silencing were assessed on day 15. The percentage of (B) matured DCs (gated on CD11c+ DC cells), (C) CD4+ and (D) CD8+ T cells (gated on CD3+CD45+ T cells), and (E) macrophages in resected bladder tumor tissues from mice intravesically instilled with PBS, OMVs, siR-OMVs, and OMV-siR robots ($n = 3$; means \pm SD). Cytokine contents in excised bladder tumor tissues from mice treated with nanorobots and other control groups: (F) IFN- γ , (G) TNF- α , and (H) IL-6 ($n = 3$; means \pm SD). (I) Western blot and (J) immunohistochemistry staining of survivin expression in resected bladder tumor tissues from mice upon intravesical administrations of nanorobots and other control groups. (Scale bar: 100 μ m.)

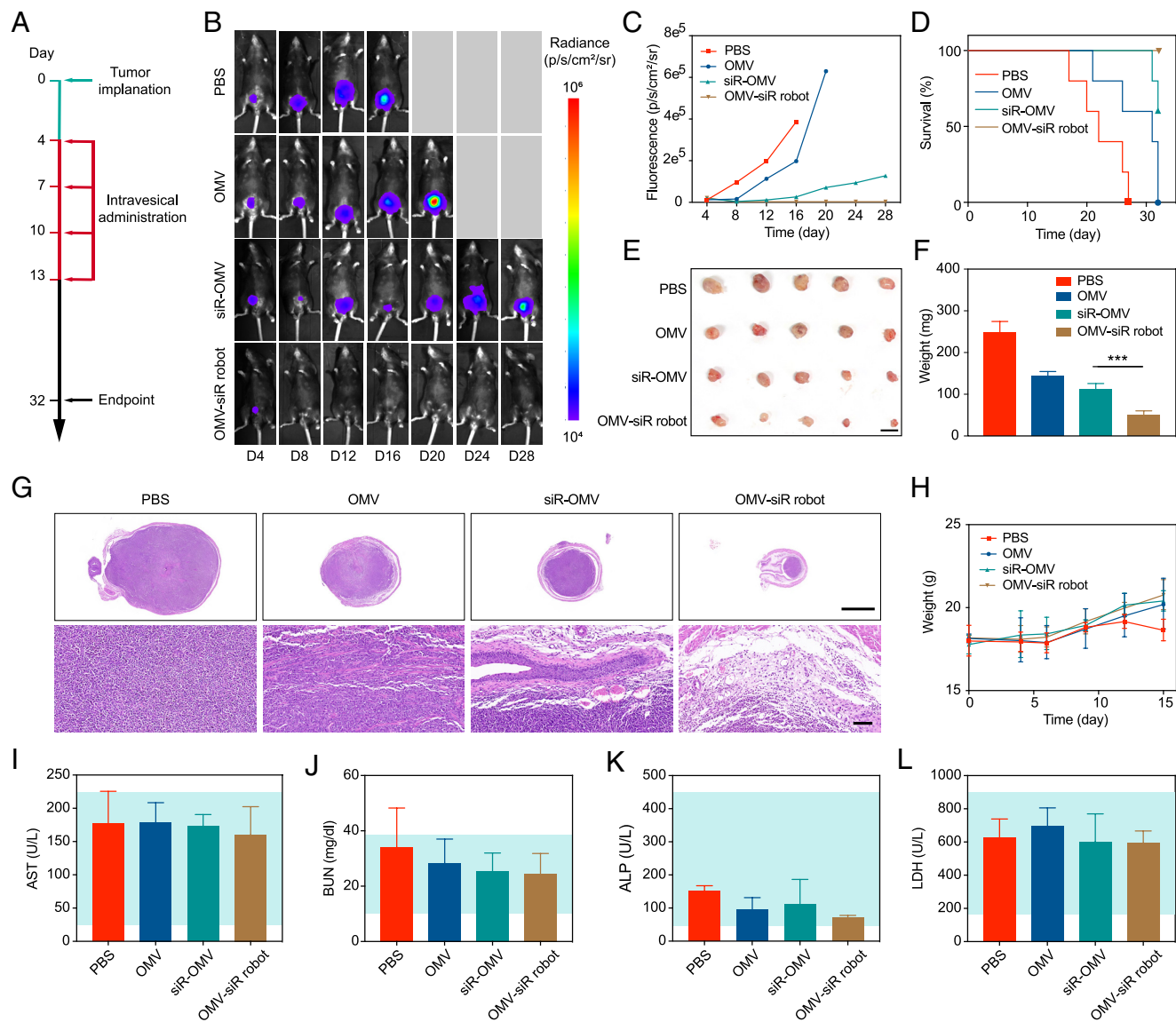


Fig. 6. In vivo antitumor effect of OMV-siR robots using an orthotopic bladder tumor model. (A) Schematic of the treatment course of mice bearing orthotopic MBT-2 bladder tumor. (B) Representative in vivo bioluminescence images of MBT-2 bladder tumor-bearing mice and (C) quantified bioluminescence intensity upon various intravesical administrations over the treatment course, including PBS, OMVs, siR-OMVs, and OMV-siR robots. (D) Survival rate of mice treated with nanorobots and other control groups over the treatment course ($n = 5$; mean \pm SD). (E) Images, (F) weights and (G) hematoxylin and eosin (H&E) staining (Top: overall view; Bottom: zoom-in view) of bladder tumor tissues from mice upon intravesical instillations of nanorobots and other control groups at the end (day 32) of treatment ($n = 5$; mean \pm SD). Scale bar, 2.5 mm for Top row and 100 μ m for the Bottom row. (H) Body weights of tumor-bearing mice upon various intravesical administrations. The expression level of serum biomarkers of tumor-bearing mice after treated with nanorobots and other control groups at the end of treatment: (I) aspartate aminotransferase (AST), (J) BUN, (K) ALP, (L) LDH ($n = 3$; mean \pm SD). *** $P < 0.001$; one-way ANOVA.

validate the favorable biosafety of OMV-siR robots for in vivo applications.

Discussion

Untethered nanorobots with controllable motion extend the operation horizon of robotic tools for various biomedical applications (48–50). However, the inadequate biocompatibility and poor biological functions of existing nanorobots have restricted their adoption and performance in the biomedical community (51). To address these issues, we developed OMV nanorobots by modifying urease on the surface of bioengineered OMVs. The integration of naturally derived OMVs and enzyme yields fully biocompatible nanorobots with intrinsic features of OMVs that other inorganic building blocks lack, including immunogenicity and surface engineering diversity for desired biofunctionalities. We demonstrated an OMV nanorobot with CPP bioengineered

surface capable of tumor targeting and penetration, as an illustrative example. The membrane structure of OMV nanorobots could effectively protect the loaded siRNA from enzymatic degradation. The biofuel urea-enabled propulsion of the nanorobots improved their binding and penetration to in vitro cell spheroid and in vivo tumor tissues within the tumor-bearing bladder. The synergistic effect of active propulsion and bioengineered CPP of nanorobots significantly enhanced the immune regulation and siRNA delivery after intravesical instillation in the animal model of orthotopic bladder tumor, further leading to the highest antitumor efficacy compared to other static groups. The produced ammonia may increase the local pH and neutralize the acidic tumor microenvironment, leading to an enhanced antitumor immune response (52, 53). Future efforts will be devoted to investigating this promising feature of urease-powered OMV nanorobots. We expect that the enzyme biocatalyst, bioengineered OMV modification, and payload of this nanorobot platform can be reconfigured to utilize

other types of enzymes and bioavailable fuels (e.g., catalase and glucose oxidase for H₂O₂ and glucose, respectively), functional proteins, and therapeutic agents [e.g., chemodrugs and oncolytic virus (54)]. The attractive versatility and adaptability of OMV nanorobots show promising potential to meet the rigorous requirements of a wide range of biomedical applications.

Materials and Methods

Bacterial Engineering and OMV Preparation. The fusion gene encoding Cytolysin A (ClyA), 6xHis, and cell-penetrating peptide (CPP) were cloned into pET28a vector (pET28a-ClyA-6xHis-CPP) for coexpression of ClyA-6xHis-CPP fusion protein. The amino acid sequence of the CPP is CGKRK (Cys-Gly-Lys-Arg-Lys). The competent *E. coli* (BL21; ZOMANBIO Corp., China) were transformed with pET28a-ClyA-6xHis-CPP. The desired bacterial colonies were selected by culturing in LB broth with kanamycin (50 µg/mL) on the shaking stage (37 °C, 180 rpm). When the optical density at 600 nm (OD₆₀₀) of the above LB broth reached 0.6 to 0.8, IPTG (0.1 mM) was added for another 14-h incubation at 16 °C to induce the fusion protein expression. Afterward, bacteria were collected by centrifugation (5,000 × g, 10 min) and redispersed in sterile PBS solution (0.2 g/mL). Next, the resulting suspension was sonicated to generate OMVs using an ultrasonic homogenizer (Scientz-11D) in the ice bath (20 min, 65 W, cycles of 3-s pulse and 5-s interval). OMVs were collected by centrifugation twice (10,000 × g, 4 °C, 20 min) and filtration through 0.2-µm polyvinylidene fluoride filters (Jet Biofil). The resulting OMV solution was further concentrated using a 100-kDa filter (Millipore) and purified by ultracentrifugation (150,000 × g, 2 h, 4 °C; XPN, Beckman Coulter). Last, the fabricated OMVs were stored in PBS solution (1 ×, pH 7.4) at –20 °C until use. The counterparts, OMV-WT were prepared using a single colony *E. coli* (BL21) without genetic engineering.

The expression of 6xHis-CPP protein in bioengineered bacteria and generated OMVs was verified by western blot analysis. The wild-type bacteria and resulting OMVs were used as control. Briefly, the bacteria or OMVs were lysed using a cell lysis buffer (Meilunbio). The protein concentration was normalized using a bicinchoninic acid assay (BCA, Meilunbio). The protein profiles were separated using SDS-polyacrylamide gel electrophoresis and transferred to polyvinylidene fluoride membrane (Millipore). After blocking, the membrane was sequentially incubated with mouse 6xHis antibody (ProteinTech) and secondary antibody (Abcam) for 1 h. The bands were visualized using GelView 6000 pro (BLT).

Fabrication of OMV-siR Robots. The fabricated OMVs (330 µL, 1.5 mg/mL, described above) were mixed with glycerin (100 µL, 50%), PBS (45 µL, 1 ×, pH 7.4), and siRNA (25 µL, 20 µM; Genepharma) for 20 min. The mixture was subsequently electroporated twice (500 V, 50, ∞) using Bio-Rad GenePulser Xcell. The resulting siRNA-loaded OMVs were concentrated and purified by concentration (5,000 × g, 1 h, 4 °C) using a 100-kDa filter (Millipore), then stored in PBS (400 µL, 1 ×, pH 7.4) at –20 °C until use.

Meanwhile, urease solution (1 mg/mL in PBS, 200 µL) was mixed with Sulfo-NHS-biotin (200 µL, 16.6 µM; Macklin) for 45 min upon gentle shaking at room temperature. The resulting urease-biotin was centrifuged (1,500 × g, 3 min) three times using a 100-kDa filter (Millipore), then stored in PBS (400 µL, 1 ×, pH 7.4) at –20 °C until use.

Afterward, siRNA-loaded OMVs (described above) were reacted with sulfo-NHS-biotin (166 µM), streptavidin (166 µM; Sigma), and urease-biotin (described above) for 45 min, respectively. To remove free agents, centrifugation with PBS was performed three times using a 100-kDa filter (Millipore) after each reaction. The resulting OMV-siR robots were stored in PBS (400 µL, 1 ×, pH 7.4) at –20 °C until use.

Characterization of OMV-siR Robots and Counterparts. The morphologies of OMV-WT, OMV-CPP, siR-OMV, and OMV-siR robots were examined by TEM using a FEI Talos F200X. The hydrodynamic size and zeta potential were evaluated using a Malvern Paralytical Zetasizer Nano ZS90.

To verify the successful loading of siRNA inside siR-OMV robots, siRNA was mixed with sulfo-Cy5-NHS ester [sulfo-NHS-Cy5, excitation (Ex)/emission (Em) = 649/667 nm; Lumiprobe] at a molar ratio of 1:2 in DEPC-treated water and reacted for 45 min at 4 °C before electroporation. OMVs were incubated with Dio

dye (1 µg/mL, Ex/Em = 487/501 nm; Beyotime) for 30 min. In another independent experiment that aims to confirm the successful modification of urease onto OMV-siR robots, urease solution was sequentially reacted with sulfo-NHS-Cy5 (1 mM) and sulfo-NHS-biotin for 30 min. OMVs were also labeled with Dio dye (1 µg/mL) for 30 min. The fluorescence images of OMV-siR robots were captured using a confocal laser scanning microscopy (CLSM, Zeiss LSM800).

The protein profiles of unmodified OMVs and OMV-siR robots were analyzed by lysing OMV membranes with cell lysis buffer (Yeasen Biotech) and conducting gel electrophoresis with Coomassie blue staining according to the manufacturer's protocol.

To examine the role of nanorobots in protecting loaded siRNA from degradation, the RNase solution (TransGen Biotech) was first diluted 500 times with distilled water to prepare the RNase working solution. 100 µL of free siRNA or OMV-siR robots at the same siRNA concentration of 0.1 nM were cultured with 10 µL of RNase working solution for various durations (0, 0.5, 1, and 2 h). Then, DNA loading buffer (Yeasen) was used to prepared samples, which were further transferred to a 1.5% agarose gel containing GelRed nucleic acid stain (SMOBIO). The agarose gel electrophoresis was conducted in 1 × tris-acetate-EDTA (Invitrogen) at 100 V for 40 min and imaged by a Bio-Rad Gel Doc XR system. The degradation test was also explored in serum-containing solution. 10 µL of free siRNA or OMV-siR robots at the same siRNA concentration of 5 nM were incubated with 100 µL of 1,640 cell culture medium containing 10% FBS for different time (0, 1, 4, and 8 h). The sample preparation and analysis were the same as described above.

Animal Care. The mice in this study were purchased from GemPharmatech Co., Ltd. All animal experiments were conducted in accordance with the guidelines and approval of Animal Use and Care Committee of Shenzhen Luohu Hospital Group.

Motion Study. The motion behaviors of OMV-siR robots were evaluated in PBS solution containing various urea concentrations (0, 50, 100, and 200 mM) or in real urine collected from mice bearing orthotopic bladder tumor. The urea concentration in mice urine was evaluated using AU5821 Clinical Chemistry Analyzer (Beckman) based on the manufacturer's protocol. In three independent experiments, the detected urea concentration was 420.5, 450.0, and 473.5 mM, with an average concentration of 448.0 ± 26.6 mM. The motion videos were captured using an inverted optical microscope with the dark-field condenser (Nikon Eclipse Ti-U) and analyzed by NIS-Elements AR software. The diffusion coefficient (D_{eff}) was calculated according to the equation, $MSD(\Delta t) = 4 D_{eff} \Delta t$, where Δt means the time interval.

The motility of nanorobots over extended periods of time was evaluated in PBS solution containing 200 mM urea over 24 h. The movement was assessed at various time points, including 0, 8, 16, and 24 h. Fresh 200 mM urea was added after 24 h.

The construction stability of nanorobots was evaluated by examining their enzyme fluorescence using a CLSM and motion capability in PBS solution containing 200 mM urea after storage for 7 d.

Survivin Expression and siRNA Selection. The expression level of survivin in various cells, including SV-HUC-1, bEnd.3, MB49, and MBT-2 cells were analyzed. Briefly, the cells were seeded in a 96-well plate (10⁴ cells per well) and incubated for 48 h. Then, the cells were harvested and lysed for western blotting analysis. The blots were labeled with survivin antibody (Cell Signaling Technology) and secondary antibody (Abcam). Actin was analyzed as the loading control.

To determine the siRNA type as the model drug, MBT-2 cells (10⁴ cells per well) were seeded in a 96-well plate and incubated overnight. Then, negative control siRNA (siRNA-NC), siRNA-257, and siRNA-810 were added and cultured for 3 d. The siRNA concentration was unified as 1 mM in 200 µL. The cell viability was examined using the Cell Counting Kit-8 (CCK-8) assay (Meilunbio) upon the manufacturer's instruction. The absorbance at 450 nm was detected using a Spark multimode microplate reader (Tecan).

siRNA Loading and Release. The loading capacity of nanorobots was explored upon various siRNA inputs (0.5, 0.75, 1, 1.5, and 3 µM in total 500 µL) in the fabrication process. The mixture of siRNA and OMVs before electroporation was first quantified using the Qubit microRNA assay (Invitrogen). After electroporation, the resulting suspension was centrifuged using a 100-kDa filter (Millipore). The bottom solution was collected to detect siRNA concentration.

The loading amount and efficacy were calculated by Eqs. 1 and 2, respectively:

$$\text{Loading amount } (\mu\text{M}) = (\text{Total amount in mixture}) - (\text{Amount in bottom solution}), \quad [1]$$

$$\text{Loading efficiency}(\%) = \frac{\text{Loading amount}}{\text{Total amount in mixture}} \times 100\%. \quad [2]$$

To assess the drug release profile, the fabricated OMV-siR robots were dispersed in 2 mL of PBS solution at pH 5.0 or 7.4. 100 μL of nanorobot solution was extracted and lysed by cell lysis buffer (1 μL ; Meilunbio) to quantify the siRNA concentration using the Qubit microRNA assay (Invitrogen), as the "original siRNA concentration." After incubation for various durations (1, 2, 3, 4, 8, and 12 h), 100 μL of solution was taken out again from the original solution to test the remaining siRNA concentration. The drug release percentage was calculated by Eq. 3:

$$\text{Release } (\%) = \frac{\text{Original siRNA} - \text{Remaining siRNA}}{\text{Original siRNA}} \times 100\%. \quad [3]$$

Cytotoxicity. SV-HUC-1, bEnd.3, and MBT-2 cells were seeded in a 96-well plate (10^4 cells per well) overnight. After removing the suspension, OMV nanorobots loaded with siRNA-NC at various concentrations (5.5, 11, 22, 44, and 88 $\mu\text{g}/\text{mL}$) were added and cultured for 48 h. The cell viability was assessed using CCK-8 assay.

In Vitro Anticancer Activity. To evaluate the impact of electroporation on loaded siRNA within nanorobots, commercial liposomes (Lipofectamine 3000; Invitrogen) were used to load siRNA, serving as the counterpart of nanorobots. The siRNA (100 pmol) was loaded inside the liposome (5 μL , siR-Lipo) through coculture in Opti-MEM medium (250 μL) without serum for 5 min at room temperature. MBT-2 cells were seeded in a 96-well plate (2×10^3 cells per well) and cultured overnight. The cells were incubated with siR-Lipo and nanorobots at the same siRNA concentration for 4 h in Opti-MEM medium, followed by isolation for another 20-h incubation in 1,640 cell culture medium. Then, MBT-2 cells were collected to examine survivin mRNA expression using quantitative PCR analysis. Total RNA was extracted using TRIzol (Invitrogen) and further analyzed using Bio-Rad CFX96 real-time PCR detection system.

To evaluate the propulsion effect on the binding efficiency between nanorobots and cells, MBT-2 cells (10^5 cells per well) were seeded in a six-well plate and cultured overnight. Afterward, siR-OMVs and OMV-siR robots (same OMV concentration of 44 $\mu\text{g}/\text{mL}$) loaded with Cy5-labeled siRNA were added and cultured in PBS containing 100 mM urea for 2 h. The OMV concentration was quantified using BCA protein assay (MeilunBio) based on the manufacturer's protocol. After three-time washing with PBS, the cells were stained with Hoechst 33342 (1 μM) for 30 min, followed by fluorescence characterization using the CLSM.

To explore the in vitro anticancer efficacy, MBT-2 cells were seeded in a 96-well plate (2×10^3 cells per well) and cultured overnight. Then, cells were incubated with various solutions containing 100 mM urea for 2 h, including PBS, siRNA, OMVs, siR-OMVs, and OMV-siR robots (OMV 44 $\mu\text{g}/\text{mL}$, 200 μL). After removing the suspension, fresh 1,640 medium was added for another 22 or 46-h incubation. The cell viabilities after incubation for 24 or 48 h were evaluated using CCK-8 assay. To further assess the cell apoptosis, MBT-2 cells were collected after 48-h incubation and suspended in annexin-V FITC binding solution (195 μL , TransGen Biotech). Next, the cells were labeled using Annexin-V-FITC/PI Apoptosis Kit (TransGen Biotech) for 20 min, followed by flow cytometry analysis (Becton Dickinson FACS Aria II). The survivin mRNA expression in MBT-2 cells was examined by quantitative PCR analysis after 24-h incubation. The expression level of survivin protein in MBT-2 cells was evaluated after incubation for 48 h. The cells were harvested and lysed for western blotting analysis. Glyceraldehyde-3-phosphate dehydrogenase (GAPDH) was employed as loading control.

Tumor Binding and Penetration. To verify the penetration capability of OMV-CPP, cell spheroids were first built by culturing MBT-2 cells in a 96-well plate with the ultralow attachment surface (10^3 cells per well) for 7 d. The resulting cell spheroids were then stained with Hoechst 33342 (1 μM , Ex/Em = 361/497 nm) for 3 h. After washing with PBS three times, Dil (Ex/Em = 549/565 nm)-labeled OMV-WT or OMV-CPP (44 $\mu\text{g}/\text{mL}$, 200 μL in PBS) were incubated with cell spheroids overnight. Then, cell spheroids were isolated and washed with PBS for

fluorescence characterization using a CLSM (Zeiss LSM800). The bladder mucosa of mice was also excised and stained with Hoechst 33342. Afterward, Dil-labeled OMV-WT or OMV-CPP (44 $\mu\text{g}/\text{mL}$, 100 μL in PBS) were added on the membrane surface for 2 h, followed by fluorescence characterization.

The binding affinity of nanorobots was evaluated by incubating with various cells, including T24, MBT-2, SV-HUC-1, and bEnd.3 cells. The cells (10^5 cells per well) were seeded in 6-well plate overnight. Then, Dil-labeled OMV nanorobots were added and cultured for 2 h in the presence of 100 mM urea. Next, the cells were washed with PBS and stained by Hoechst 33342 (1 μM) for fluorescence characterization.

To examine the tissue binding and penetration of nanorobots, cell spheroids were first built by culturing MBT-2 cells in a 96-well plate with the ultralow attachment surface (10^3 cells per well) for 12 d. Dil-labeled siR-OMV or OMV-siR robots (44 $\mu\text{g}/\text{mL}$, 200 μL in PBS) were cultured with Hoechst 33342-labeled cell spheroids in the presence of 100 mM urea for 2 h. The fluorescence images of cell spheroids were captured using CLSM.

In vivo evaluation was conducted using mice bearing orthotopic MBT-2 bladder tumor, established by injecting luciferase-expressing MBT-2 cells (10^5 cells) into the bladder cavity via a 31G \times 6 mm insulin syringe (Becton, Dickinson and Company). Twelve days after the cell inoculation, the tumor-bearing mice were randomly divided to 3 groups and intravesically instilled with Dil-labeled urease-modified OMV-WT, siR-OMVs, and OMV-siR robots (44 $\mu\text{g}/\text{mL}$, 100 μL) through a closed IV catheter system (0.7 mm \times 19 mm, BD Intima II). The bladders were collected after incubation for 2 or 12 h. The bladder tumor tissues were sliced to stain with Hoechst 33342 for fluorescence characterization.

In Vivo Antitumor Study. To explore the immune stimulation and gene silencing of OMV-siR robots, the mice bearing orthotopic MBT-2 bladder tumor were first established by injecting luciferase-expressing MBT-2 cell (10^5 cells) into the bladder cavity as described above (day 0). Four days after cell inoculation (day 4), the tumor-bearing mice were randomly divided to four groups ($n = 5$) and intravesically instilled with PBS, OMVs, siR-OMVs, and OMV-siR robots (44 $\mu\text{g}/\text{mL}$, 50 μL in PBS). A closed IV catheter system (0.7 mm \times 19 mm, BD Intima II) was inserted through the urethra and into the bladder. The inserted length of the catheter was around 16 mm. The solution (50 μL) was manually injected in 10 s. The duration of intravesical instillation was 1 h, where the mice were anesthetized in this process. Such administration was performed every 3 d with a total of four treatments. At day 15, the mice were killed to harvest the tumor tissues. The collected tumor tissues were first processed with immunohistochemistry staining to examine the expression of proinflammatory cytokines (TNF- α , IL-6, and IFN- γ) and survivin protein. The expression level of proinflammatory cytokines was analyzed by software Fiji. To evaluate the phenotype of immune cells, the bladder tumor tissues were cut into small pieces (around 1 mm to 3 mm) and digested by collagenase I/IV in DMEM for 30 min. The tissue residuals were removed by filtration (40- μm mesh cell strainer, Jet Biofil) and centrifugation (12,000 \times g, 5 min). Next, the lysis buffer was added to the suspension to remove unwanted red blood cells, followed by twice wash with PBS containing 1% (w/v) BSA. Afterward, various antibodies were added for flow cytometry analysis. Among them, CD45-PerCP-Cyanine5.5 (45-0451-80), CD3-FITC (11-0032-82), CD8a-PE (12-0081-82), and CD4-APC (17-0042-81) were added to assess T cells. The mature DCs were examined by adding CD11c-FITC (11-0114-81), CD86-PE (12-0862-81), and CD80-APC (17-0801-81). The macrophage phenotype was evaluated by staining with CD11b-PerCP-Cyanine5.5 (45-0112-80), F4/80-FITC (11-4801-82), and CD206-PE (12-2061-80). These antibodies were purchased from eBioscience Inc. (San Diego, USA). The resulting suspension was also used to explore the expression level of survivin by western blotting analysis. Actin was used as the loading control.

To assess the antitumor effect of OMV-siR robots, the mice bearing orthotopic bladder tumor were established and performed the same intravesical administration as described above. The orthotopic tumor growth was monitored by the bioluminescence of inoculated luciferase-expressing MBT-2 cell every 4 d using an AniView100 multimode animal live imaging system (BLT) since day 4. The survival rate and body weight of mice were also recorded during the treatment course. The mice were killed at the endpoint of treatment (day 32). Then, the bladders were excised for histological staining, including H&E, TUNEL, and Ki67.

To evaluate the biosafety, the serum samples of mice were collected at day 32 before being killed. The serum biomarkers, AST, ALT, BUN, ALP, and LDH

were detected by a Biochemical Autoanalyzer (Chemray 800, Rayto). The major organs, including the heart, liver, spleen, lung, and kidney, were resected for H&E staining.

Statistical Analysis. Quantitative data are illustrated as means \pm SD or means \pm SEM. Comparison between multiple groups was performed using one-way ANOVA with a Tukey post hoc test. Statistical significance is represented as * P < 0.05; ** P < 0.01; *** P < 0.001; **** P < 0.0001.

Data, Materials, and Software Availability. All study data are included in the article and/or supporting information.

ACKNOWLEDGMENTS. We acknowledge the experimental supports from Shenzhen Research Institute of Wuhan University. This work was funded by Shenzhen Science and Technology Innovation Commission (RCJC20200714114557005),

National Natural Science Foundation of China (61931024, 92359202), Sanming Project of Medicine in Shenzhen (SZSM202211009), and Shenzhen Science and Technology Program (JCYJ20220818100015031, JCYJ20220530151408018).

Author affiliations: ^aInstitute of Urology, The Third Affiliated Hospital of Shenzhen University, Shenzhen 518000, People's Republic of China; ^bAndrew and Peggy Cherg Department of Medical Engineering, California Institute of Technology, Pasadena, CA 91125; ^cSouth China Hospital, Health Science Center, Shenzhen University, Shenzhen 518116, People's Republic of China; ^dLuohu Clinical Institute of Shantou University Medical College, Shantou University Medical College, Shantou 515000, People's Republic of China; and ^eDepartment of General Surgery, Shenzhen Samii Medical Center, Shenzhen 518118, People's Republic of China

Author contributions: S.T., D.T., Y.L., W.G., and S.W. designed research; S.T., D.T., H. Zhou, Y.L., D.Z., X.P., C.R., Y.S., S.Z., H. Zheng, F.W., J.Y., H.H., and X.M. performed research; S.T., D.T., and W.G. analyzed data; and S.T., D.T., W.G., and S.W. wrote the paper.

1. P. L. Venugopalan, B. Esteban-Fernandez de Avila, M. Pal, A. Ghosh, J. Wang, Fantastic voyage of nanomotors into the cell. *ACS Nano* **14**, 9423–9439 (2020).
2. Z. Wu, Y. Chen, D. Mukasa, O. S. Pak, W. Gao, Medical micro/nanorobots in complex media. *Chem. Soc. Rev.* **49**, 8088–8112 (2020).
3. X. Peng *et al.*, Autonomous metal-organic framework nanorobots for active mitochondria-targeted cancer therapy. *Sci. Adv.* **9**, eadh1736 (2023).
4. F. Novotny, H. Wang, M. Pumera, Nanorobots: Machines squeezed between molecular motors and micromotors. *Chem* **6**, 867–884 (2020).
5. J. Law *et al.*, Micro/nanorobotic swarms: From fundamentals to functionalities. *ACS Nano* **17**, 12971–12999 (2023).
6. J. Wang, Z. Xiong, J. Zheng, X. Zhan, J. Tang, Light-driven micro/nanomotor for promising biomedical tools: Principle, challenge, and prospect. *Acc. Chem. Res.* **51**, 1957–1965 (2018).
7. S. Yu, Y. Cai, Z. Wu, Q. He, Recent progress on motion control of swimming micro/nanorobots. *View* **2**, 20200113 (2021).
8. S. Sengupta, M. E. Ibele, A. Sen, Fantastic voyage: Designing self-powered nanorobots. *Angew. Chem. Int. Ed.* **51**, 8434–8445 (2012).
9. M. Yang, X. Guo, F. Mou, J. Guan, Lighting up micro-/nanorobots with fluorescence. *Chem. Rev.* **123**, 3944–3975 (2022).
10. Y. Dong *et al.*, Magnetic helical micro-/nanomachines: Recent progress and perspective. *Matter* **5**, 77–109 (2022).
11. Y. Zhang, H. Hess, Chemically-powered swimming and diffusion in the microscopic world. *Nat. Rev. Chem.* **5**, 500–510 (2021).
12. A. D. Fusi *et al.*, Achieving control in micro-/nanomotor mobility. *Angew. Chem. Int. Ed.* **62**, e202214754 (2023).
13. V. M. Kadiri *et al.*, Biocompatible magnetic micro- and nanodevices: Fabrication of fept nanopropellers and cell transfection. *Adv. Mater.* **32**, 2001114 (2020).
14. M. Zhou *et al.*, Cancer cell membrane camouflaged semi-yolk@spiky-shell nanomotor for enhanced cell adhesion and synergistic therapy. *Small* **16**, 2003834 (2020).
15. B. Esteban-Fernández de Ávila *et al.*, Single cell real-time mirnas sensing based on nanomotors. *ACS Nano* **9**, 6756–6764 (2015).
16. Y. Chen *et al.*, Carbon helical nanorobots capable of cell membrane penetration for single cell targeted sers bio-sensing and photothermal cancer therapy. *Adv. Funct. Mater.* **32**, 2200600 (2022).
17. M. Yan *et al.*, Site-selective superassembly of biomimetic nanorobots enabling deep penetration into tumor with stiff stroma. *Nat. Commun.* **14**, 4628 (2023).
18. J. Gao *et al.*, Hyperthermia-triggered biomimetic bubble nanomachines. *Nat. Commun.* **14**, 4867 (2023).
19. J. Guo, J. J. Gallegos, A. R. Tom, D. Fan, Electric-field-guided precision manipulation of catalytic nanomotors for cargo delivery and powering nanoelectromechanical devices. *ACS Nano* **12**, 1179–1187 (2018).
20. A. C. Hortelao *et al.*, Swarming behavior and in vivo monitoring of enzymatic nanomotors within the bladder. *Sci. Robot.* **6**, eabd2823 (2021).
21. X. Ma, A. C. Hortelao, A. Miguel-Lopez, S. Sanchez, Bubble-free propulsion of ultras-small tubular nanojets powered by biocatalytic reactions. *J. Am. Chem. Soc.* **138**, 13782–13785 (2016).
22. A. Terzopoulou *et al.*, Metal-organic frameworks in motion. *Chem. Rev.* **120**, 11175–11193 (2020).
23. I. Ortiz-Rivera, M. Mathesh, D. A. Wilson, A supramolecular approach to nanoscale motion: Polymersome-based self-propelled nanomotors. *Acc. Chem. Res.* **51**, 1891–1900 (2018).
24. M. Wan *et al.*, Bio-inspired nitric-oxide-driven nanomotor. *Nat. Commun.* **10**, 966 (2019).
25. M. Wan, T. Li, H. Chen, C. Mao, J. Shen, Biosafety, functionalities, and applications of biomedical micro/nanomotors. *Angew. Chem. Int. Ed.* **60**, 13158–13176 (2021).
26. Y. Zhou *et al.*, Stimuli-responsive functional micro-/nanorobots: A review. *ACS Nano* **17**, 15254–15276 (2023).
27. B. E.-F. de Ávila *et al.*, Hybrid biomembrane-functionalized nanorobots for concurrent removal of pathogenic bacteria and toxins. *Sci. Robot.* **3**, eaat0485 (2018).
28. C. Simo *et al.*, Urease-powered nanobots for radionuclide bladder cancer therapy. *Nat. Nanotechnol.* **19**, 554–564 (2024).
29. Q. Long *et al.*, Engineered bacterial membrane vesicles are promising carriers for vaccine design and tumor immunotherapy. *Adv. Drug Deliv. Rev.* **186**, 114321 (2022).
30. C. Schwechheimer, M. J. Kuehn, Outer-membrane vesicles from gram-negative bacteria: Biogenesis and functions. *Nat. Rev. Microbiol.* **13**, 605–619 (2015).
31. M. Kaparakis-Liaskos, R. L. Ferrero, Immune modulation by bacterial outer membrane vesicles. *Nat. Rev. Immunol.* **15**, 375–387 (2015).
32. M. Li *et al.*, Bacterial outer membrane vesicles as a platform for biomedical applications: An update. *J. Control. Release* **323**, 253–268 (2020).
33. L. Agemy *et al.*, Targeted nanoparticle enhanced proapoptotic peptide as potential therapy for glioblastoma. *Proc. Natl. Acad. Sci. U.S.A.* **108**, 17450–17455 (2011).
34. J. A. Hoffman *et al.*, Progressive vascular changes in a transgenic mouse model of squamous cell carcinoma. *Cancer Cell* **4**, 383–391 (2003).
35. T. Patino *et al.*, Influence of enzyme quantity and distribution on the self-propulsion of non-janus urease-powered micromotors. *J. Am. Chem. Soc.* **140**, 7896–7903 (2018).
36. X. Zhao, K. Gentile, F. Mohajerani, A. Sen, Powering motion with enzymes. *Acc. Chem. Res.* **51**, 2373–2381 (2018).
37. S. Tang *et al.*, Enzyme-powered janus platelet cell robots for active and targeted drug delivery. *Sci. Robot.* **5**, eaba6137 (2020).
38. V. Sridhar *et al.*, Carbon nitride-based light-driven microswimmers with intrinsic photocharging ability. *Proc. Natl. Acad. Sci. U.S.A.* **117**, 24748–24756 (2020).
39. B. Yang, L. Bankir, Urea and urine concentrating ability: New insights from studies in mice. *Am. J. Physiol. Renal Physiol.* **288**, F881–F896 (2005).
40. D. C. Altieri, Validating survivin as a cancer therapeutic target. *Nat. Rev. Cancer* **3**, 46–54 (2003).
41. X.-H. Lai *et al.*, Cytocidal and apoptotic effects of the clyA protein from *Escherichia coli* on primary and cultured monocytes and macrophages. *Infection Immunity* **68**, 4363–4367 (2000).
42. S. N. Wai *et al.*, Vesicle-mediated export and assembly of pore-forming oligomers of the enterobacterial clyA cytotoxin. *Cell* **115**, 25–35 (2003).
43. Q. Hu *et al.*, Cgkrk-modified nanoparticles for dual-targeting drug delivery to tumor cells and angiogenic blood vessels. *Biomaterials* **34**, 9496–9508 (2013).
44. S. K. Williams, D. M. Hoening, R. Ghavamian, M. Soloway, Intravesical therapy for bladder cancer. *Expert Opin. Pharmacother.* **11**, 947–958 (2010).
45. J. Zhou *et al.*, Physical disruption of solid tumors by immunostimulatory microrobots enhances antitumor immunity. *Adv. Mater.* **33**, 2103505 (2021).
46. K. Cheng *et al.*, Bioengineered bacteria-derived outer membrane vesicles as a versatile antigen display platform for tumor vaccination via plug-and-display technology. *Nat. Commun.* **12**, 2041 (2021).
47. O. Y. Kim *et al.*, Bacterial outer membrane vesicles suppress tumor by interferon- γ -mediated antitumor response. *Nat. Commun.* **8**, 626 (2017).
48. J. Li, B. E.-F. de Ávila, W. Gao, L. Zhang, J. Wang, Micro/nanorobots for biomedicine: Delivery, surgery, sensing, and detoxification. *Sci. Robot.* **2**, eaam6431 (2017).
49. M. Lian *et al.*, Movable hollow nanoparticles as reactive oxygen scavengers. *Chem* **5**, 2378–2387 (2019).
50. M. Pal *et al.*, Maneuverability of magnetic nanomotors inside living cells. *Adv. Mater.* **30**, 1800429 (2018).
51. B. Wang, K. Kostarelos, B. J. Nelson, L. Zhang, Trends in micro-/nanorobotics: Materials development, actuation, localization, and system integration for biomedical applications. *Adv. Mater.* **33**, 2002047 (2020).
52. L. Zhang *et al.*, Efficient immunotherapy of drug-free layered double hydroxide nanoparticles via neutralizing excess acid and blocking tumor cell autophagy. *ACS Nano* **16**, 12036–12048 (2022).
53. N. Yang *et al.*, Magnesium galvanic cells produce hydrogen and modulate the tumor microenvironment to inhibit cancer growth. *Nat. Commun.* **13**, 2336 (2022).
54. S. J. Russell, K. W. Peng, J. C. Bell, Oncolytic virotherapy. *Nat. Biotechnol.* **30**, 658–670 (2012).